

A Measure of Active Interfaces in Supported Catalysts for High-temperature Reactions

Siwon Lee

Korea Advanced Institute of Science and Technology

Hyunwoo Ha

Chungnam National University <https://orcid.org/0000-0002-3874-8669>

Kyung Taek Bae

Korea Advanced Institute of Science and Technology

Seunghyun Kim

Korea Advanced Institute of Science and Technology

Hyuk Choi

Chungnam National University

Jun Hyuk Kim

Korea Advanced Institute of Science and Technology

Jongsu Seo

Korea Advanced Institute of Science and Technology

Jin Choi

Korea Advanced Institute of Science and Technology

Yong-Ryun Jo

Gwangju Institute of Science and Technology

Bong-Joong Kim

Gwangju Institute of Science and Technology <https://orcid.org/0000-0002-5335-4342>

Kang Taek Lee

Korea Advanced Institute of Science and Technology

Hyun You Kim

University of Texas at Austin

WooChul Jung (✉ wchung@kaist.ac.kr)

Korea Advanced Institute of Science and Technology <https://orcid.org/0000-0001-5266-3795>

Article

Keywords: heterogeneous catalysis, metal-gas interfaces, metal-oxide-gas interfaces, three dimensional, reaction pathways

Posted Date: March 11th, 2021

DOI: <https://doi.org/10.21203/rs.3.rs-182805/v1>

License:  This work is licensed under a Creative Commons Attribution 4.0 International License.
[Read Full License](#)

Version of Record: A version of this preprint was published at Chem on December 1st, 2021. See the published version at <https://doi.org/10.1016/j.chempr.2021.11.024>.

Abstract

Formulating knowledge of structure-function relationships in heterogeneous catalysis is central to the rational design of highly efficient catalysts, yet the elucidation of dominant reaction sites has remained as a grand challenge for researchers. Here, we present a novel methodology that can be used to visualize metal-gas and metal-oxide-gas interfaces in three dimensions and to quantify their catalytic activity levels. As a case study, CH₄ oxidation occurring in a Pt/CeO₂ system is chosen. By employing thermally robust Pt@CeO₂ model catalysts with size-tunable and monodisperse cores, and gas-permeable shells, we reconstruct a series of heterogeneous structures in 3D via electron tomography and match the information precisely to catalytic activity data and theoretical calculations. This strategy reveals that the two different interfaces concurrently catalyze the CH₄ oxidation and that their contribution to the overall reaction rate changes dynamically with respect to the Pt size, temperature, and gas atmosphere. Our results provide a new analytic platform on which to explore reaction pathways and mechanisms applicable to multiple reactions and materials.

Main Text

The interplay between oxide supports and supported metal nanoparticles is of high significance in the field of heterogeneous catalysis¹⁻⁵. While the role of oxides was oversimplified in the past, evidence suggests that the use of redox-active oxides (such as CeO₂, ceria) as a support material can dramatically reshape the landscape of multiple high-value catalytic processes⁶⁻¹⁴. Often, the augmented catalytic activity is attributed to the synergistic interaction between the metal and the support, as the overall rate of reaction can be much greater than the sum of the rates over the support and the metal individually¹⁵. Therefore, many studies including CO oxidation and water-gas-shift reactions have been dedicated to unraveling the roles of such interfaces¹⁶⁻²⁰. As such, it is implied that the strong local electronic and structural interactions at metal-support interfaces may improve the inherent catalytic activity of supported metal species²¹. Other studies have also indicated that such metal-support interactions provide more reactive sites by facilitating interface-mediated reaction paths^{2,8,22,23}.

While the aforementioned studies have produced valuable insights regarding the functions of metal-support interfaces, nevertheless, it should be noted that the overall turnover rate may not entirely be determined by the metal-support interface. In other words, the surfaces of metal particles are still likely to be involved in the bigger picture, even when active supports are used. Generally, for supported metal catalysts, the rate of the overall chemical reaction is primarily determined by the elemental steps that occur at either the double-phase boundary (2PB) between the gas and the metal or the triple-phase boundary (3PB) at which the gas, metal, and oxide support phase are simultaneously in contact. Indeed, the extent to which each reaction site contributes to the overall reaction rate likely depends on the type of reaction²⁴ and/or the catalyst composition^{25,26}. Furthermore, the dominant reaction site and pathway, even for the same reaction and material, can vary dynamically according to the temperature²⁷, ratio of the reactants^{28,29}, and the microstructure of the catalyst (i.e., the size distribution of the supported metal

nanoparticles)^{30,31}. To date, however, few studies have attempted to quantify the competition between these two interfaces. Therefore, it has never been possible to answer the following fundamental questions, which can be a substantial cornerstone in the design of an ideal catalyst: “Which of the two interfaces of a given catalyst is more active depending on the reaction, temperature and gas atmosphere?” and “How exactly is that interface more important than the other, numerically?”

To this end, two major issues must be resolved; first, the density of each active site (i.e., 2PB and 3PB) should be accurately characterized and controlled; thereafter, the catalytic activity of interest should be monitored carefully in relation to the variant ratio of 2PB and 3PB. In this vein, Cargnello et al. successfully determined how the frequency of atoms at 2PB and 3PB varies with the particle size *via* imaging of the structures of monodispersed metal nanocrystals dispersed on ceria supports. They reported that the change in the CO oxidation rate according to the particle size coincided with the change in the number of atoms at 3PB, which unambiguously demonstrated that the metal-ceria interface is the only active site for CO oxidation in the measurement condition they studied³².

Despite the fact that the approach described above represents one of the most triumphant cases of compiling size-activity relationships in heterogeneous catalysis, the temperature window in that study was below the calcination temperature (< 573 K), whereas many industrially important chemical reactions proceed at high temperatures (> 773 K). Indeed, the coarsening and coalescence of nanosized metal particles are likely to occur at elevated temperatures³³, posing a particular challenge with regard to maintaining the density of each active site (i.e., the 3PB length and 2PB area per gram of metal used). Methane activation, one of the most treasured reactions for the academy as well as the enterprise, is a typical example of a high-temperature reaction. In particular, this reaction is of interest because specific target applications (i.e., combustion *vs.* reforming) require different operating conditions (i.e., temperatures, types of oxidant, CH₄-to-oxidant ratios) and the corresponding reaction pathways are therefore expected to vary markedly. Cargnello et al. demonstrated that enhanced metal-support interactions can lead to outstanding methane combustion rates in Pd@CeO₂ subunits³⁴. Zhang et al. reported that the interfacial site between Co and CeO₂ is essential for the catalytic reaction during the dry reforming of methane³⁵. Previous studies have identified the possibility that the metal-ceria interface may play a role in methane activation, yet no attempt has been made to quantify the roles of 2PB and 3PB sites individually over a wide range of temperatures and gas atmospheres. Therefore, a novel strategy is essential to overcome the morphological evolution of catalysts at high temperatures and thus to assess the value of each key reaction site, which is much more challenging.

In this study, we present thermally stable and oxide-encapsulated metal catalysts with well-defined geometries and reaction sites. Size-tunable monodisperse Pt nanoparticles surrounded by a gas-permeable ceria shell are selected as a model catalyst. For comparison, silica-encapsulated Pt catalysts are prepared as a reference for inert support. Electron tomography (ET) combined with a three-dimensional (3D) reconstruction method is then utilized directly to observe and quantify the Pt-gas and Pt-CeO₂-gas interfaces. Based on these corresponding results, we measure how the 2PB and 3PB site

densities (per gram of Pt) vary with the particle size and how the catalytic activities for CH₄ oxidation change accordingly. The two reaction sites participate simultaneously in CH₄ oxidation, and the contribution of each reaction site to the overall reaction rate is identified, which is further supported by the theoretical interpretation that corroborates the dual-site reaction pathways for methane oxidation in a ceria-Pt system. Our results suggest a reliable platform with which to explore catalytically active sites and pathways for various chemical reactions even at high temperatures.

Monodisperse Pt NPs having four different diameters were prepared through aqueous-based colloidal synthesis using a cationic surfactant³⁶. Transmission electron microscopy (TEM) bright field (BF) images show that the particles are 7.8 ± 0.8 , 9.1 ± 0.5 , 11.8 ± 1.6 , and 19.7 ± 1.7 nm in size, respectively (**Figs. 1a to 1d**). Subsequently, the Pt NPs were encapsulated with gas-permeable thin layers of ceria (**Figs. 1e to 1h**) or silica (**Figs. 1i to 1l**) to prevent coalescence at elevated temperatures. The electrostatic interaction between cationic Pt NPs and anionic Ce precursor complex ions helps cerium oxide shell overcoat Pt NPs uniformly³⁷, which is manifested in the energy dispersive spectroscopy (EDS) mapping (**Fig. S1**). Moreover, scanning electron microscopy (SEM) and TEM BF images at low magnifications confirm that individual Pt NPs are encapsulated in ceria shells (**Fig. S2**). The CeO₂ crystallites in the outer layer of the core-shell structure were approximately 6 nm in size, corresponding to the calculated value from the X-ray diffraction peaks (**Fig. S3**). The fabricated Pt@CeO₂ structures were later evenly dispersed on additional high-surface-area ceria supports ($78 \text{ m}^2 \text{ g}^{-1}$), utilizing the opposite surface charges (**Figs. S4 and S5**). In a similar manner, Pt@SiO₂ samples were prepared by the hydrolysis and condensation of Si precursors around Pt NPs and the subsequent polymerization of silicates, as has been demonstrated elsewhere^{38,39}. For all of the samples, we kept the thickness of the ceria and silica shell constant at approximately 20 nm and 30 nm, respectively, by adjusting the reaction time so as to eliminate the effects of shell thickness variations on the measured catalytic activities.

These shell configurations demonstrate the capability of effectively inhibiting the structural evolution of the catalysts during high-temperature annealing. **Fig. 2** shows a series of TEM BF images obtained while annealing a Pt@CeO₂ sample at elevated temperatures (**Figs. 2a-d**) and at prolonged times (**Figs. 2d-f**), demonstrating that the Pt@CeO₂ catalysts maintain their morphology without coarsening of Pt NPs up to 873 K. The as-synthesized Pt NPs showed faceted forms due to different growth rates of Pt NP along $\langle 100 \rangle$ and $\langle 111 \rangle$ directions⁴⁰, but as the temperature increased, the shape of the Pt NPs became spherical with random orientations (**Fig. S6-S8**). The ceria shell also retained its porosity without aggregation. Another important factor to consider is that catalysts can undergo structural evolution on the atomic scale, such as single atom (SA) formation, during a high-temperature heat treatment⁴¹⁻⁴⁴. In particular, the Pt-CeO₂ system has been reported to favor the atomic-scale dispersion of Pt during oxidative high-temperature calcination. However, we did not observe any noticeable modifications after calcination at 873 K (**Fig. S9**). Perhaps different catalytic configurations, such as the initial morphology and composition of the catalyst, influenced the process of structural transformation. Similar to Pt@CeO₂, Pt@silica was also stable up to 873 K while maintaining its core-shell structure (**Fig. S6**).

Next, we visualized the Pt@CeO₂ catalysts in three dimensions through electron tomography. For 3D reconstruction, samples before and after a heat treatment at 873 K were utilized, and the cubic voxels of all samples had a side length of 1~2 Å. The 3D resolution of the tomogram was calculated based on the Fourier shell correlation (FSC) with a criterion of 0.143 (**Fig. S10**), showing an average value of 1.28 ± 0.19 nm. This value is close to the resolution limit (approximately 1 nm) achievable for a 60 nm object at 1° tilt increments based on the Crowther-Klug criterion⁴⁵. We note that in our study, the core-shell catalysts had a size in the range of 50 to 60 nm, and the tilt increment for tomography data acquisition was 1°. Each resolution for the nine different samples used in this study is summarized in **Table S1**. To quantify the microstructural properties in 3D, including the density of the 2PB and 3PB sites, we applied a semi-automated segmentation routine to the tomograms (**Fig. S11**). **Fig. 3a** shows the resultant 3D reconstruction image, indicating that the Pt particle is uniformly surrounded by a mesoporous ceria shell, which is readily accessible to gas molecules. A cross-sectional view of the core-shell catalyst along the Z-axis also shows pores between 1.6 and 3.7 nm in size inside the ceria shell (**Fig. S12**). **Figs. 3b and 3c** visually identify the 3PB (red line) and 2PB (green phase) sites, respectively. The 3D tomogram results shown in **Video S1** display the morphology and the internal structure of the object, a series of core-shell catalysts, improving our structural understanding of the samples. **Table S2** presents quantified results showing how each reaction site density normalized to the Pt loading amount depends on the diameter (d) of the Pt NPs. As the particle size decreases, the density of the 2PB and 3PB sites increases, but different tendencies arise according to the value of d . For example, the density of the two sites in the Pt@CeO₂ composites shows power-law exponents of -1.02 ± 0.12 and -1.88 ± 0.26 , respectively, for d (**Figs. 3d and 3e**). Advanced ET technology has recently begun to be applied to heterogeneous catalytic research, but it has only been used to qualitatively confirm the porous structure, and it is noteworthy that this is *the first report* to quantify key reaction sites of nanocomposite catalysts through ET^{46,47}. As will be discussed later, the scale relationships between the two reaction site densities with respect to d reflect the respective reaction rates.

Before an in-depth discussion of CH₄ activation on the model catalyst system, the validity of the 3D tomography analysis and the reconstruction process must be ensured; hence, we carried out ad hoc CO chemisorption and oxidation analyses with the Pt@CeO₂ catalysts. First, the 2PB site density was directly measured *via* CO chemical adsorption, taking into account the property by which CO molecules are selectively adsorbed on the Pt surface. **Table S3** shows the exposed metal surface area (EMSA) per unit mass of the Pt@CeO₂ catalysts *vs. d*. Thereafter, the 3PB density was reliably deduced using CO oxidation as a reference reaction. Earlier results demonstrated that the ceria-Pt interface is the dominant reaction site for CO oxidation in the conditions used in this study³². Accordingly, the power-law dependence of CO oxidation reactivity on d is expected to reflect that of the 3PB interface in our catalytic system. Indeed, the kinetic results of CO oxidation on the Pt@CeO₂ system are identical to those when the ceria-Pt interface is a dominant reaction site in the Pt/CeO₂ system. Moreover, the core-shell catalyst with a high 3PB density has a higher reaction rate than the supported-Pt catalyst, indicating that the 3PB site is an active site (see details in **Figs. S13 and S14**). **Fig. S15** shows the changes of the 2PB and 3PB site density levels

extracted by additional adsorption and oxidation experiments according to the diameter and with power-law exponents for d of -0.93 ± 0.02 and -1.95 ± 0.02 , respectively. It turns out that the image analyses and experimental supporting results are in good agreement within a standard deviation of 7%. This in combination with the fact that the pore sizes of the ceria shell as judged by tomography are in line with the pore-size distribution obtained *via* the adsorption experiments clearly demonstrates that our analytic approach is solid³⁷. In sum, this judicious design of a composite catalyst enables the quantification of idealized 2PB and 3PB interfaces for chemical reactions while effectively suppressing the agglomeration of metal cores at high temperatures; this is of key importance when constructing an analytic platform to find the dominant reaction site for a given catalytic reaction.

Next, we evaluated the activity of CH₄ oxidation on oxide-encapsulated Pt NP catalysts as a case study for typical high-temperature reactions. CH₄ oxidation is a fundamental reaction for various industrial applications, such as catalytic combustion, emission control, and hydrogen reforming^{34,48}, but the reaction mechanisms within the ceria-Pt system have not yet been fully identified. The kinetic rate data for CH₄ oxidation over ceria- and silica-encapsulated Pt NPs are shown in **Fig. 4a** and **Fig. S16**. First, the Pt@SiO₂ catalysts used as an inert support reference always exhibit a constant reaction rate regardless of the particle size when normalized to 2PB as determined by CO chemisorption (**Fig. S16**). In contrast, the Pt encapsulated with a reducible CeO₂ support (Pt@CeO₂) exhibited directly opposite behavior, as the reaction rate strongly depends on the particle size (**Fig. 4a**). This implies that in addition to the Pt surface, another reaction site, plausibly the ceria-Pt interface, acts as a reaction area in the ceria-Pt system. Because the increase in the 3PB density is more pronounced than that of the 2PB density as the size of the Pt dwindles, it is anticipated that the role of the 3PB site is emphasized with tiny Pt NPs. Indeed, as the Pt size decreases, the apparent values of E_a gradually decrease from 82.8 to 63.8 kJ mol⁻¹, signifying that the dominant active site adapts with the catalyst size.

Reaction orders for CH₄ and O₂ will present a clearer understanding of the role of the Pt-ceria interface in CH₄ oxidation reactions. For silica-based catalysts, an increase in the partial pressure of methane, p_{CH_4} , accelerates the reaction, whereas an increase in p_{O_2} slows down the reaction with reaction order values of 0.95 and -0.40, respectively, for CH₄ and O₂ (**Fig. S17**). These reaction order values are in good agreement with the reported values, meaning that the Langmuir-Hinshelwood-type of reaction path represents the surface reaction between adsorbed CH₄ and O₂ on Pt sites^{49,50}. In the ceria-based sample, however, relatively weak dependence of the reaction rate to p_{CH_4} and p_{O_2} was noted, with corresponding reaction orders of 0.55 in CH₄ and -0.19 in O₂; thus, it is obvious that methane combustion occurs through a reaction pathway different from that associated with silica-based catalysts. Similarly, less sensitive dependency of the catalytic activity on the partial pressure of the reactants was observed in the ethane, propane, and butane oxidation reactions on ceria-supported noble metal catalysts⁵⁰. Given the ability of ceria as an oxygen reservoir, these results can be explained by the dual-function mechanism in which the ceria supplies oxygen to the supported metal and the delivered oxygen interacts with methane provided near the Pt-ceria interface^{50,51}. The presence of Pt indeed activates lattice oxygen atoms in the

vicinity of the ceria surface and reduced the activation energy for the dissociative adsorption of methane^{23,52}. Thus, the aforementioned results consistently represent the principal evidence of the active role of Pt-ceria interfacial sites regarding CH₄ oxidation, while their degree of participation may vary with the particle size.

The values of the turnover rate as a function of the catalyst diameter can be considered as more direct and decisive evidence specifying the predominant interface, whereas the plot can be further deconvoluted to quantify the accurate ratio of reaction engagement between 2PB and 3PB. The overall reaction rate comes from scaling relationships for CH₄ oxidation, described in the form of a double-logarithmic plot (log TOF vs. log d). For the Pt@silica samples, we found that the TOFs for CH₄ oxidation were proportional to $d^{-0.51\pm0.36}$, which is consistent with the trend of EMSA, which varies with d (EMSA $\propto d^{-0.54\pm0.18}$) (**Fig. S18**). This observation corroborates the contention that CH₄ combustion occurs dominantly at the Pt surface sites of the Pt@silica catalysts, which is further supported by the fact that the reaction rate normalized by EMSA is independent of d (**Fig. S16**). In contrast, the tendency of the change in the TOF in the Pt@ceria samples is not always consistent with the trend of the 2PB site density variation according to the value of d (**Fig. 4b**); rather, the power-law dependence of d for TOF exists between those of 2PB and 3PB. Therefore, the TOF values of CH₄ oxidation could be fitted using two parallel relationships, as plotted in **Figs. 4b-d**, showing the TOF value vs. d (i.e., TOF $\propto C_1d^{-1.02} + C_2d^{-1.88}$, where C_1 and C_2 are constant.). These data fitting results reveal that both active sites concurrently contribute to the methane oxidation reaction and allocate their proportion under the given reaction condition. For example, as shown in **Fig. 4b and Table S4**, when d is 10 nm, the reaction temperature is set to 823 K, and the O₂/CH₄ ratio of the input gas is 4, it can be found that 2PB and 3PB are almost equally important and partake in the overall reactivity at rates of 45% and 55%, respectively.

Based on these scaling relation results, we can quantify how each interface contributes to the overall TOF value according to the Pt particle size, temperature, and gas composition (ratio between CH₄ and O₂). In terms of d , the smaller the particle size, the greater the number of sites at the Pt/ceria interface relative to the surface area of Pt exposed at a given mass, meaning that the overall reactivity of the core-shell catalysts is determined more by an elemental process at 3PB. On the other hand, for larger NPs, 2PB dominates the overall reaction. As shown in **Table S4**, the role of 3PB increases rapidly from 15% to 90% as the size of Pt decreases from 100 nm to 1 nm at 823 K with an O₂/CH₄ ratio of 4. In addition, because the elemental steps in 2PB and 3PB have different activation energies (~ 100 kJ mol⁻¹ and ~ 60 kJ mol⁻¹, respectively), the contribution of each interface varies with the temperature. For example, the 3PB interface plays a more dominant role at the lower temperature of 723 K as compared to the role at 823 K if all other factors (e.g., the feed gas ratio and Pt NP size) are equal (**Figs. 4b-c and Tables S4-S5**). These results indicate that the metal-ceria interface density must be maximized to achieve CH₄ activation at lower temperatures, consistent with earlier findings in the literature^{25,53}.

In addition to the particle size and temperature effects, the dominant active region also varies with the gas composition introduced. As shown in **Fig. 4d**, if the reaction occurs at an O_2/CH_4 ratio of 0.0625 (oxygen-lean condition), 2PB contributes entirely to the overall TOF values. In contrast, 3PB dominates the overall catalytic activity at a higher O_2/CH_4 ratio of 40 (oxygen-rich condition). These reactant-gas-dependent catalytic responses arise from the difference in the predominantly adsorbed species on the Pt NPs depending on the O_2/CH_4 ratio⁵⁴. At higher relative oxygen ratios, more oxygen covers the Pt surface, with intimate Pt-O interactions. The preferred oxygen saturation suppresses CH_4 adsorption on the Pt surface and thus the participation of 2PB accordingly. This reduces the overall activity (**Fig. S19**); however, it makes the participation of 3PB relatively important. Methane oxidation at 2PB, on the other hand, plays an important role during oxygen-lean conditions. Eventually, combining the robust model catalytic system and a quantitative analysis of nanoscale interfaces, we directly observed the dual-site reaction mechanism toward high-temperature CH_4 oxidation under various reaction conditions.

To clarify the mechanistic details pertaining to the roles of 2PB and 3PB, we performed DFT calculations. Two types of structural models are utilized to model CH_4 oxidation on core-shell Pt@CeO₂ comprehensively: a conventional Pt₉ NP on CeO₂(100) and an inverse Ce₇O₁₄ NP on Pt(111). Here, only the energetics from the former system is presented because relatively consistent results were deduced from both systems (refer to SI for additional data pertaining to the latter model). The calculated binding energy, E_{bind} , of CH_4 (-0.44 eV) and O_2 (-2.14 eV) molecules on Pt NPs indicates that the Pt NP preferentially binds to O_2 initially (**Fig. S20**). Because subsequent dissociation of the Pt-bound O_2 molecule is exothermic with a low E_a , we initially saturated the Pt NPs of Pt@CeO₂ models with oxygen (**Fig. S20**). Later, the O-saturated Pt NP dissociatively adsorbs a CH_4 molecule in the presence of the pre-adsorbed oxygen atoms (a1 and b1, **Fig. 5**), initiating the subsequent CH_4 oxidation steps. Although both the Pt-CeO₂ interface (3PB) and the surface Pt (2PB) can bind to CH_4 , 3PB is energetically more preferred (**Fig. 5**). Moreover, 3PB provides greater thermodynamic driving force for the sequential dehydrogenation of CH_4 (**Fig. 5**), suggesting that 3PB is the primary CH_4 activation site at low CH_4 concentrations. Interestingly, both 2PB and 3PB sites show high E_a values for the dehydrogenation of CH_4 (**Figs. S21 and S22**). However, considering that the reaction occurs at a high temperature and that the entropic contribution to the energetics of CH_4 dissociation provides additional driving force for hydrogen abstraction overall, these E_a values will not hinder the reaction. The DFT-estimated subsequent dissociative adsorption of CH_4 and dehydrogenation of CH_3^* (**Fig. 5**) show that Pt-bound oxygen atoms, Pt-O*, accept the abstracted hydrogen atoms from CH_4 and release them as H₂O (see **Figs. S21 and S22** for more details). The formation and release of the first H₂O molecule on the 2PB and 3PB sites proceed rapidly (a3-4 and b3-4, **Fig. 5**). Although the release of the second H₂O from 2PB or 3PB requires an E_{de} value of 0.49 eV or 0.86 eV, respectively (a7 and b7, **Fig. 5**), a large portion of E_{de} can be supplied by the positive (qualitatively) entropic contribution to the Gibbs free energy of H₂O desorption.

The remaining C of CH₄ was combined with two different oxygen species: Pt-O* (2PB) or lattice oxygen of CeO₂ (3PB), being transformed into Pt-CO* (a5 and b5, **Fig. 5**). These two oxygen species concurrently contribute to the overall CO₂ production rate because their E_a values of CO₂ formation are nearly identical (**Figs. S21 and S22**). The comparable E_{de} values of CO₂ from 2PB (0.41 eV) and 3PB (0.55 eV) predict that both are energetically available (a9 and b9, **Fig. 5**). Supporting our experimental prediction, that Pt@ceria provides at least two active sites for CH₄ oxidation, the DFT calculation results describe the dual-site reaction pathways in a condition in which O₂ covers the Pt surface, similar to the actual environment. Because no notable relative superiority of a specific site was found, the relative ratio of 2PB and 3PB, a direct function of the size of the Pt NPs, steers the dominant reactive species and the pathway for CH₄ oxidation.

In sum, we showcased a generalizable empirical and characterization framework with which to determine the dominant reaction sites in the Pt-CeO₂ system with regard to methane oxidation, a crucial reaction proceeding at elevated temperatures. In contrast to recent reports that narrowly focused on the roles of redox-active supports, we found that the primary reaction sites between 2PB and 3PB vary with extreme sensitivity according to the temperature, gas pressure, and the size of the metal NPs. Particularly, empowered by a combination of a theory-based mechanistic study and state-of-the-art experimental synthesis and analysis, we revealed that a larger NP size, an increasing *T* value and a decreasing *p*O₂ value lead to a greater contribution of 2PB to the total methane turnover rate, and vice versa, marking, *for the first time*, the development of a quantitative direct relationship between the areal fraction of the reaction sites and the catalytic activity of metal NPs toward high-temperature chemical reactions. The aforementioned strategy may globally guide other metal-catalyst support systems for a variety of industrially important reactions, and the new insights gained here present a roadmap with which to find the 'ideal catalyst' for a specific target condition.

Method

Synthesis of Pt nanoparticles

An aqueous solution of potassium tetrachloroplatinate(II) (10 mM, 5 mL) and alkyltrimethylammonium bromide (C_{*n*}TAB, *n* = 12, 14, 16 and 18) (400 mM, 12.5 mL) was added to 29.5 mL of deionized (DI) water while being stirred. The mixture was then heated to 323 K for 20 min. When using the C₁₈TAB surfactant, the mixture was heated to 328 K for 25 min due to its greater hydrophobicity. Subsequently, a reduction agent, sodium borohydride (500 mM, 3mL), was injected into the mixture. Hydrogen gas formed in the flask was released into the fume hood for 20 min using a syringe needle. The mixture solution was then aged at 323 K for 15 h under magnetic stirring. The mixture including the C₁₈TAB surfactant was aged at 328 K for 15 h. Afterward, the resulting solution was centrifuged at an appropriate rpm to clean up the as-synthesized Pt nanoparticles (NPs). For the Pt NPs capped by C₁₈TAB (i.e., x-small sized Pt), 10 mL of ethanol was added to the resulting solution and the mixture was then centrifuged at 12,000 rpm for 60 min. After removing the supernatant, a volume of DI water equal to that of the removed supernatant was

added and this was centrifuged again at 12,000 rpm for 60 min. For the Pt NPs capped by C₁₆TAB (i.e., small-sized Pt), the resulting solution was subjected to centrifugation at 3,000 rpm for 30 min. Then, the supernatant was mixed with 10 mL of ethanol, after which centrifugation took place at 12,000 rpm for 30 min. For the Pt NPs capped by C₁₄TAB (i.e., medium-sized Pt), the resulting solution was subjected to centrifugation at 3,000 rpm for 30 min. Subsequently, the supernatant was separated and centrifuged again at 12,000 rpm for 15 min twice. For the Pt NPs capped by C₁₂TAB (i.e., large-sized Pt), the resulting solution was centrifuged at 6,000 rpm for 15 min. The precipitate at the bottom of the centrifuge tube was collected and dispersed in DI water (5 mL) for further use.

Synthesis of Pt@CeO₂ nanostructures

The as-synthesized C_nTAB (n = 12, 14, 16, and 18)-capped Pt NPs at a level of 0.5 mL were blended with an aqueous solution of C₁₄TAB (25 mM, 40 mL). For the C₁₂TAB-capped Pt NPs, 0.75 mL of a colloidal solution of Pt NPs was used. The Pt concentration of each solution is compiled in **Table S3**. To cover the surface of the Pt NPs with a precursor containing Ce ions, aqueous solutions of EDTA-NH₃ and Ce(NO₃)₃•6H₂O were prepared, as follows. For the preparation of the EDTA-NH₃ solution, concentrated ammonia (0.38 mL, 28~30 wt%) was mixed with an aqueous solution of EDTA (10 mM, 40 mL). An aqueous solution of Ce(NO₃)₃•6H₂O (100 mM, 10 mL) was prepared by dissolving the Ce(NO₃)₃•6H₂O precursor in DI water, after which 3 mL of EDTA-NH₃ and 0.3 mL of Ce(NO₃)₃•6H₂O solutions were injected into the mixture solution of Pt and C₁₄TAB. After shaking the mixture gently for 1 min, it was thermally aged at 363 K for 8 h. The resulting cloudy brown solution was subjected to centrifugation at 8000 rpm for 10 min and the final precipitate was collected and dispersed in DI water (10 mL) for further use.

Synthesis of Pt@silica nanostructures

The as-synthesized C_nTAB (n = 12, 14, 16, and 18)-capped Pt NPs at a level of 0.5 mL were dispersed in an aqueous solution of C₁₄TAB (10 mM, 40 mL for x-small, small, and medium size Pt NPs; 12.5 mM, 40 mL for large size Pt NPs). To the C₁₄TAB-stabilized Pt NPs solution, concentrated ammonia (0.1 mL, 28~30 wt%) was added to keep the pH level at 10~11. In order to form a silicon oxide shell around the dispersed Pt NPs, 10 vol% of TEOS diluted with ethanol (3 mL for x-small and small, 4 mL for medium, and 5 mL for large Pt NPs) was added. The mixture was left under stirring for 1h to allow oxide encapsulation to occur. The resulting cloudy brown solution was centrifuged at 12000 rpm for 15 min and the final precipitate was collected and dispersed in DI water (1 mL) for further use.

Preparation of the Pt(1 wt%)@CeO₂/ CeO₂ catalysts

A suitable amount of CeO₂ support was dispersed in a basic solution to prepare the surface of CeO₂ to have a negative charge. The cerium oxide support was prepared by the calcination of Ce(NO₃)₃•6H₂O in air at 723 K for 20 h. Based on the ICP-OES results shown in **Table S3**, we prepared an appropriate

amount of a Pt@CeO₂ synthetic solution so that the amount of Pt was adjusted to 1 wt% to the total weight of the catalyst. Then, a concentrated ammonia solution (0.38 mL, 28~30 wt%) was added to make the surface of the core-shell structure negative. C₁₄TAB (10 mM) was added to the Pt@CeO₂ solution so that the surface charge of the core-shell structure would be positive (**Fig. S4** and **Table S6**). Each mixture solution (CeO₂ support and Pt@CeO₂) was mixed together with stirring at 300 rpm for 10 minutes. The resulting solution was centrifuged at 8000 rpm for 10 min and the precipitate was collected and dried at 353 K overnight. The as-synthesized Pt(1 wt%)@CeO₂/CeO₂ catalyst was calcined at 623 K for 5h in air to eliminate the residual organics, such as C_nTAB, EDTA, and ethanol, and to lead to the formation of pores in the cerium oxide shell. The wt% of Pt NPs in the final catalysts was reconfirmed by means of an X-ray fluorescence (XRF) analysis. The surface charge of each species was verified *via* a zeta-potential measurement. The zeta-potential measurement and XRF results are compiled in **Table S6** and **Table S7**, respectively.

Preparation of the Pt(1 wt%)/CeO₂ catalysts

A suitable amount of CeO₂ support was dispersed in a basic solution to prepare the surface of CeO₂ to impart a negative charge. We then prepared a proper amount of a colloidal solution consisting of positively charged Pt NPs so as to adjust the amount of Pt to 1 wt% of the total weight of the catalyst (the Pt concentration was verified by ICP-OES and is compiled in **Table S3**). Each solution (CeO₂ support and Pt NPs) was mixed under stirring at 300 rpm for 10 minutes. The resulting solution was then centrifuged at 8000 rpm for 10 min and the precipitate was collected and dried at 353 K overnight. The as-synthesized Pt(1 wt%)/CeO₂ catalyst was calcined at 623 K for 5 h in air. The wt% of the Pt NPs in the final catalysts was confirmed by an XRF analysis (**Table S7**).

Preparation of the Pt(1 wt%)@silica/silica catalysts

A suitable amount of silicon oxide support was dispersed in a basic solution to prepare the surface of silica to have a negative charge. Based on the ICP-OES results shown in **Table S3**, we prepared an appropriate amount of a positively charged Pt@silica synthetic solution so that the amount of Pt was adjusted to 1 wt% of the total weight of the catalyst. Each solution (silica support and Pt@silica) was mixed while being stirred at 500 rpm for 30 minutes. Afterward, the mixture was separated into the supernatant liquid and the precipitate. The supernatant liquid was removed and the precipitate was dried at 353 K overnight. The as-synthesized Pt(1 wt%)@silica/silica catalyst was calcined at 723 K for 3 h in air to remove the residual organics, such as C_nTAB, TEOS, and ethanol, leading to the formation of pores in the silica shell.

Catalytic performance tests

CH₄ and CO oxidation

A fixed-bed micro-reactor with a 4 mm inner diameter was used to measure the catalytic activity of the CH₄ and CO oxidation processes. To create the catalyst bed, 50 mg of a catalyst was mixed with 100 mg of quartz sand and this was then placed between layers of quartz wool. To ensure that neither mass nor heat transfer limitations affected the measured results, we performed the conversion while changing the flow rate at a constant space velocity, finding that the conversion characteristics remained constant (**Fig. S23**). The feeds for CH₄ oxidation (composed of 0.5 vol% CH₄ and 2 vol% O₂ in an Ar balance) and CO oxidation (composed of 1 vol% CO and 4 vol% O₂ in an Ar balance) were passed through the reactor. To investigate the effect of the feed gas ratio, we adjusted the input gas ratio (O₂/CH₄) from 0.0625 (oxygen-lean condition) to 40 (oxygen-rich condition). The total flow rate was 50 mL min⁻¹ for both oxidation reactions. The reaction rate was recorded while increasing the temperature with a ramping rate of 3 K min⁻¹. For each test, the catalyst was activated in the reaction environment at 873 K for CH₄ oxidation and 573 K for CO oxidation. The gas concentration change was detected with a quadrupole mass spectrometer (Pfeiffer Vacuum GSD320) in real time. The CH₄ and CO conversion ratios (%) were defined as the ratio of the converted reactant to the total input reactant (i.e., CH₄ conversion ratio = 100 × (mol CH_{4, inlet} - mol CH_{4, outlet})/mol CH_{4, inlet}; CO conversion ratio = 100 × (mol CO_{, inlet} - mol CO_{, outlet})/mol CO_{, in}). To rule out the effect of the CeO₂ support itself toward CH₄ oxidation, we subtracted the reaction rate of the CeO₂ support from the overall measured reaction rate so as to determine the reaction rate associated with Pt NPs. The reaction orders for CH₄ and O₂ were determined as follows. For the reaction order of CH₄, the reaction rate was measured by varying the partial pressure of CH₄ (*p*CH₄) (from 2 × 10⁻³ to 6 × 10⁻³ atm) while keeping the partial pressure of O₂ (*p*O₂) constant at 5 × 10⁻² atm. In the same way, for the reaction order of O₂, we determined the reaction rate according to the change in *p*O₂ (from 1 × 10⁻² to 5 × 10⁻² atm) while keeping the *p*CH₄ constant at 2 × 10⁻³ atm. To investigate the reaction order of CO and O₂, we measured the reaction rate by changing the partial pressure of carbon monoxide (*p*CO) (from 1 × 10⁻³ to 6 × 10⁻³ atm) while holding the *p*O₂ level at 5 × 10⁻² atm. We also carried out rate measurements according to the *p*O₂ variation while keeping the *p*CO level at 1 × 10⁻³ atm. Methane gas was detected by the *m/z* = 15 peak instead of the 16 peak to avoid interference from the fragments of CO, CO₂, H₂O, and O₂. The CO gas signal was measured by taking into account the contribution from CO₂ gas via the mass concentration determination (MCD) mode.

Characterization techniques

The morphologies and elemental compositions of the synthesized core-shell catalysts were characterized by means of bright-field transmission electron microscopy (TEM) and energy-dispersive X-ray spectroscopy (EDX) (JEOL JEM-3010 operating at 300kV and FEI Talos F200X operating at 200kV), respectively. Catalyst powder samples were drop-casted onto lacey carbon films on copper grids (Electron Microscopy Sciences) from concentrated ethanol and then dried in an oven at 343 K for 10 min. For *in-situ* heating TEM observations, we used an in-situ heating holder (Gatan 652 double tilt) with a TEM (FEI Tecnai G2 F30 S-Twin and JEOL JEM-3011 HR) operating at 300kV. For the acquisition of the electron

tomography series, we used a tomography holder (Fischion Model 2020 Advanced Tomography Holder) with a TEM (FEI Talos F200X) operating at 200kV and with an aberration-corrected TEM (FEI Titan Cubed G2 60-300) operating at 300kV. Catalysts were drop-casted onto a silicon nitride (SiN) membrane with 0.5 1.5 mm² aperture on 200 μm silicon (Ted Pella, Inc.) and then dried in a vacuum chamber (75 Torr) at 323 K overnight. A pre-heat treatment of the catalyst for electron tomography was carried out using an *in-situ* heating TEM (FEI Tecnai G2 F30 S-Twin). Scanning electron microscopy (SEM) images were acquired using a Hitachi S-4800 device. The Pt NP concentrations in the solutions and the Pt/Ce molar ratios of the core-shell particles were determined by an inductively coupled plasma mass spectrometer (Agilent ICP-OES 720) and an X-ray fluorescence spectrometer (Rigaku ZSX Primus II). For ICP-OES, samples were dissolved in aqua regia and diluted prior to the measurement. The average particle size was calculated by counting more than 200 individual particles. The surface charge of the samples was characterized using a zeta potential analyzer (Otsuka ELS-Z2). The crystal structure of the samples was identified by powder X-ray diffraction using a Rigaku D/Mas-2500 device with Cu-Kα radiation at 40kV and 200mA with a scan rate of 4° per minute from 20° to 60°. CO chemisorption experiments were conducted on a Micromeritics ASAP 2020. The samples were placed in a U-shaped quartz reactor, heated under flowing O₂ (5%) in helium at 723 K for 1 h, reduced in flowing H₂ (5%) in helium at 423 K for 1 h, and then evacuated at 573 K for 4 h. CO chemisorption experiments performed at room temperature. Nitrogen adsorption/desorption isotherms were carried out at the temperature of liquid nitrogen (77K) using a Micromeritics Tristar II 3020 instrument to identify the pore size distribution, pore volume, and total surface area of the samples.

Electron tomography

Tilt-series high-angle annular dark-field scanning transmission electron microscope (HAADF STEM) images were acquired over an angular range of ±60° at increments of 1° at the KAIST Analysis and Research center. Alignment and the subsequent reconstruction process were carried out using FEI Inspect 3D. For the reconstruction, the simultaneous iterative reconstruction technique (SIRT)⁵⁵ with 25 iterations was used. This technique is widely used in many electron tomography processes⁵⁶⁻⁵⁹. Compared to the conventional back-projection algorithm, it can reduce spurious artifacts and enhance the contrast of reconstructed samples⁶⁰. However, technical limitation such as the finite tilting angle of the specimen holder can lead to artifacts, collectively known as the ‘missing wedge’ problem⁶¹⁻⁶³. This problem can cause elongated features along the perpendicular direction of the rotation axis (z-direction). The elongation factor can be calculated from the maximum tilt angle (α) as follows:⁶²

$$e = \sqrt{\frac{\alpha + \sin \alpha \cos \alpha}{\alpha - \sin \alpha \cos \alpha}} \quad (1)$$

The factor obtained from Eq. (1) is 1.55 when α = 60°. For an accurate imaging analysis and for proper quantification, the z-direction voxel size of the reconstructed sample was adjusted considering the elongation factor.

Segmentation process

In order to quantify the significant morphological features of size-tunable catalysts, a segmentation process of designating each phase (Pt, Ceria and pore) was utilized in a semi-automated manner. This approach proceeds with the initial use of a threshold with de-noising and contrast-enhanced filtering. Correction is then undertaken manually. To enhance the effect of post processing, background areas outside of the region of interest (ROI) are removed by a binary mask. Through this process, only the Pt@ceria catalyst remains, with the remaining pixels set to zero. Then, image de-noising is done using an anisotropic diffusion filter⁶⁴. This reduces the noise without diluting the intensity of the edges. Anisotropic diffusion filtering is known as an effective tool for de-noising and edge preservation of electron tomography fields⁶⁵⁻⁶⁷. Designating each phase was mostly performed using the Watershed segmentation algorithm⁶⁸ to minimize manual intervention. This algorithm computes the gradient of the voxel and considers it as a 2D or 3D landscape. In order to distinguish each phase from the contour of the Pt nanoparticles more precisely, adaptive histogram equalization filtering was used⁶⁹. This process enhances the contrast between phases and makes it easier to distinguish between the pores and solid phase by hand.

Quantification process

Based on the segmented data, the morphological features of the catalyst, including the particle diameter, 2PB and 3PB, were quantified with an Avizo Fire device (FEI Company). The calculated values are summarized in **Table S2**. To quantify the diameter of Pt nanoparticles and the exposed metallic surface area, the phase volume and surface area were calculated by converting the surface of the specific phase voxel into a triangular mesh. This method is a more accurate approach for calculating a three-dimensional surface compared to a voxel counting algorithm. From the quantified surface area and volume of spherical Pt nanoparticles, the particle size can be determined by the Brunauer-Emmett-Teller (BET) formula, $D=6 \times V/S$ ^{70,71}. To calculate the triple-phase boundary length, the voxels intersected with three phases (Pt, ceria, and pore phase) were extracted. The triple-phase boundary length was calculated by extracting all voxels in contact with Pt, ceria, and the pore. These extracted voxels were “skeletonize”⁷² to obtain the length, and the total length was divided by the mass of the Pt particle to yield the 3PB site density.

3D Resolution estimation

The spatial resolution of the reconstructed sample was estimated using the Fourier shell correlation (FSC) with a criterion of 0.143^{73,74}, which correlates the reciprocal-space densities of the two sub-tomograms. For this purpose, the tilt series images were separated into two groups based on odd or even numbers of the order of the tilt angles. Each group was independently reconstructed, and their 3D volumes were used to compute the FSC curves as a function of the spatial frequency in the Fourier space. The resolution was determined as the value at which the FSC curve intersected with the pre-established threshold criterion. The resolution estimation process was performed in Matlab using an in-house code.

Density functional theory calculations

We modeled the CeO₂(100) surface using a 3 × 3 supercell with three O-Ce-O triple layers. Quality test results confirmed that two key energy values, the oxygen vacancy formation energy from the 3PB and the oxygen binding energy on the 2PB, were well described with our supercell compared with a larger supercell, (5 × 5). A Pt NP composed of nine atoms was supported on the optimized CeO₂(100) substrate and repeatedly optimized upon the sequential adsorption of a total of six oxygen atoms to describe the catalyst structure under the CH₄ oxidation conditions. The bottom ceria triple-layer structure was fixed during all calculations to ensure structural robustness. An inverse Ce₇O₁₄/Pt(111) model was constructed by optimizing a Ce₇O₁₄ cluster on a 7 × 7 × 4 Pt(111) slab (**Fig. S24**). The Supplementary Information (**Figs. S25 and S26**) section provides information about the CH₄ oxidation pathways and corresponding energetics calculated from the Ce₇O₁₄/Pt(111) model. We performed spin-polarized DFT calculations using a plane-wave basis with the VASP code⁷⁵ and the PBE functional⁷⁶. The DFT+U⁷⁷ scheme with U_{eff} = 5 eV⁷⁸ was applied for Ce ions to consider the localized Ce-*f* orbitals appropriately. The interaction between the ionic core and the valence electrons was described by the projector augmented wave method⁷⁹. Valence electron wave functions were expanded in a plane-wave basis up to an energy cutoff of 400 eV. The Brillouin zone was sampled at the Γ -point for all calculations. The convergence criteria for the electronic structure and the atomic geometry were 10⁻⁴ eV and 0.03 eV/Å, respectively. We used a Gaussian smearing function with a finite temperature width of 0.05 eV in order to improve the convergence of states near the Fermi level. The location and energy of transition states (TSs) were calculated with the climbing-image nudged-elastic-band method⁸⁰.

Declarations

Acknowledgements

S. Lee, S. Kim, J. H. Kim, J. Seo and W. Jung were supported financially by grants from the National Research Foundation of Korea (NRF) and the KAIST Institute of Technology Value Creation, Industry Liaison Center (G-CORE Project) funded by the Korean government (MSIT) (NRF-2017M3A7B4049547, NRF-2019R1A2C2006006, NRF-2021M3H4A1A01002695, and N11210015). H. Ha, H. Choi, and H. Y. Kim were supported financially by a grant from the National Research Foundation of Korea (NRF) funded by the Korean government (MSIT) (NRF-2019R1A2C1089256). K. T. Bae and K. T. Lee were supported financially by grants from the National Research Foundation of Korea (NRF) funded by the Korean government (MSIT) (NRF-2019M3E6A1103944, NRF-2020R1A2C2010690, and NRF-2021M3H4A1A01002695). This research used the resources of the Center for Functional Nanomaterials, which is a U.S. DOE Office of Science Facility, and the Scientific Data and Computing Center, a component of the Computational Science Initiative, at Brookhaven National Laboratory (Contract No. DE-SC0012704). The National Institute of Supercomputing and the Network/Korea Institute of Science and Technology Information (KSC-2019-CRE-0210) also provided computing time.

Author Contributions

S. Lee and W. Jung conceived of the idea for this study. S. Lee prepared and characterized the catalysts. H. Ha and H. Choi performed the DFT calculations. K. T. Bae conducted the reconstruction and quantification of the catalysts. S. Kim synthesized the Pt@SiO₂ catalysts and collected the associated activity data. J. H. Kim and J. Seo assisted in the preparation of the catalysts. J. S. Choi supported collecting TEM data for tomography. Y-R. Jo and B-J. Kim supported collecting *in-situ* TEM data. W. Jung, H. Y. Kim, and K. T. Lee supervised the project and wrote the manuscript, and all authors commented on the data and the manuscript. S. Lee, H. Ha, and K. T. Bae equally contributed to this work.

Competing financial interests

The authors declare no competing financial interests.

Data availability

The data that support the finding of this study are available in the article and its Supplementary Information. Additional data are available from the corresponding author on reasonable request.

References

- 1 Kattel, S., Ramirez, P. J., Chen, J. G., Rodriguez, J. A. & Liu, P. CATALYSIS Active sites for CO₂ hydrogenation to methanol on Cu/ZnO catalysts. *Science* **355**, 1296+, doi:10.1126/science.aal3573 (2017).
- 2 Choi, Y. *et al.* Unravelling inherent electrocatalysis of mixed-conducting oxide activated by metal nanoparticle for fuel cell electrodes. *Nature Nanotechnology* **14**, 245+, doi:10.1038/s41565-019-0367-4 (2019).
- 3 Farmer, J. A. & Campbell, C. T. Ceria Maintains Smaller Metal Catalyst Particles by Strong Metal-Support Bonding. *Science* **329**, 933-936, doi:10.1126/science.1191778 (2010).
- 4 Kwak, N. W. *et al.* In situ synthesis of supported metal nanocatalysts through heterogeneous doping. *Nature Communications* **9**, doi:10.1038/s41467-018-07050-y (2018).
- 5 Jo, Y.-R. *et al.* Growth Kinetics of Individual Co Particles Ex-solved on SrTi_{0.75}Co_{0.25}O_{3-δ} Polycrystalline Perovskite Thin Films. *J. Am. Chem. Soc.* **141**, 6690-6697, doi:10.1021/jacs.9b01882 (2019).
- 6 Fu, Q., Weber, A. & Flytzani-Stephanopoulos, M. Nanostructured Au-CeO₂ catalysts for low-temperature water-gas shift. *Catal. Lett.* **77**, 87-95, doi:10.1023/a:1012666128812 (2001).
- 7 Rodriguez, J. A. *et al.* Activity of CeO_x and TiO_x nanoparticles grown on Au(111) in the water-gas shift reaction. *Science* **318**, 1757-1760, doi:10.1126/science.1150038 (2007).

- 8 Green, I. X., Tang, W. J., Neurock, M. & Yates, J. T. Spectroscopic Observation of Dual Catalytic Sites During Oxidation of CO on a Au/TiO₂ Catalyst. *Science* **333**, 736-739, doi:10.1126/science.1207272 (2011).
- 9 Park, J. B. *et al.* Gold, Copper, and Platinum Nanoparticles Dispersed on CeO_x/TiO₂(110) Surfaces: High Water-Gas Shift Activity and the Nature of the Mixed-Metal Oxide at the Nanometer Level. *J. Am. Chem. Soc.* **132**, 356-363, doi:10.1021/ja9087677 (2010).
- 10 Kim, K. *et al.* A Simple Descriptor to Rapidly Screen CO Oxidation Activity on Rare-Earth Metal-Doped CeO₂: From Experiment to First-Principles. *Acs Applied Materials & Interfaces* **9**, 15449-15458, doi:10.1021/acsami.7b01844 (2017).
- 11 Kayaalp, B. *et al.* Template-free mesoporous La^{<inf>0.3</inf>}Sr^{<inf>0.7</inf>}Fe^{<inf>x</inf>}Ti^{<inf>1-x</inf>}O^{<inf>3±Δ</inf>} with superior oxidation catalysis performance. *Applied Catalysis B: Environmental* **245**, 536-545, doi:10.1016/j.apcatb.2018.12.077 (2019).
- 12 Montini, T., Melchionna, M., Monai, M. & Fornasiero, P. Fundamentals and Catalytic Applications of CeO₂-Based Materials. *Chemical Reviews* **116**, 5987-6041, doi:10.1021/acs.chemrev.5b00603 (2016).
- 13 Rodriguez, J. A., Grinter, D. C., Liu, Z. Y., Palomino, R. M. & Senanayake, S. D. Ceria-based model catalysts: fundamental studies on the importance of the metal-ceria interface in CO oxidation, the water-gas shift, CO₂ hydrogenation, and methane and alcohol reforming. *Chemical Society Reviews* **46**, 1824-1841, doi:10.1039/c6cs00863a (2017).
- 14 Sun, C. W., Li, H. & Chen, L. Q. Nanostructured ceria-based materials: synthesis, properties, and applications. *Energy & Environmental Science* **5**, 8475-8505, doi:10.1039/c2ee22310d (2012).
- 15 An, K. *et al.* Enhanced CO Oxidation Rates at the Interface of Mesoporous Oxides and Pt Nanoparticles. *J. Am. Chem. Soc.* **135**, 16689-16696, doi:10.1021/ja4088743 (2013).
- 16 Chen, A. L. *et al.* Structure of the catalytically active copper-ceria interfacial perimeter. *Nature Catalysis* **2**, 334-341, doi:10.1038/s41929-019-0226-6 (2019).
- 17 Percira-Hernandez, X. I. *et al.* Tuning Pt-CeO₂ interactions by high-temperature vapor-phase synthesis for improved reducibility of lattice oxygen. *Nature Communications* **10**, doi:10.1038/s41467-019-09308-5 (2019).
- 18 Daelman, N., Capdevila-Cortada, M. & Lopez, N. Dynamic charge and oxidation state of Pt/CeO₂ single-atom catalysts. *Nat. Mater.* **18**, 1215+, doi:10.1038/s41563-019-0444-y (2019).
- 19 Yao, S. Y. *et al.* Atomic-layered Au clusters on α-MoC as catalysts for the low-temperature water-gas shift reaction. *Science* **357**, 389-393, doi:10.1126/science.aah4321 (2017).

- 20 Nie, L. *et al.* Activation of surface lattice oxygen in single-atom Pt/CeO₂ for low-temperature CO oxidation. *Science* **358**, 1419-1423, doi:10.1126/science.aao2109 (2017).
- 21 van Deelen, T. W., Hernández Mejía, C. & de Jong, K. P. Control of metal-support interactions in heterogeneous catalysts to enhance activity and selectivity. *Nature Catalysis* **2**, 955-970, doi:10.1038/s41929-019-0364-x (2019).
- 22 Bruix, A. *et al.* A New Type of Strong Metal–Support Interaction and the Production of H₂ through the Transformation of Water on Pt/CeO₂(111) and Pt/CeO_x/TiO₂(110) Catalysts. *J. Am. Chem. Soc.* **134**, 8968-8974, doi:10.1021/ja302070k (2012).
- 23 Vayssilov, G. N. *et al.* Support nanostructure boosts oxygen transfer to catalytically active platinum nanoparticles. *Nat. Mater.* **10**, 310-315, doi:10.1038/nmat2976 (2011).
- 24 Foppa, L. *et al.* Contrasting the Role of Ni/Al₂O₃ Interfaces in Water-Gas Shift and Dry Reforming of Methane. *J. Am. Chem. Soc.* **139**, 17128-17139, doi:10.1021/jacs.7b08984 (2017).
- 25 Liu, Z. Y. *et al.* In Situ Investigation of Methane Dry Reforming on Metal/Ceria(111) Surfaces: Metal-Support Interactions and C-H Bond Activation at Low Temperature. *Angew. Chem. Int. Ed.* **56**, 13041-13046, doi:10.1002/anie.201707538 (2017).
- 26 Corral-Perez, J. J. *et al.* Decisive Role of Perimeter Sites in Silica-Supported Ag Nanoparticles in Selective Hydrogenation of CO₂ to Methyl Formate in the Presence of Methanol. *J. Am. Chem. Soc.* **140**, 13884-13891, doi:10.1021/jacs.8b08505 (2018).
- 27 Liu, A. N. *et al.* Getting Insights into the Temperature-Specific Active Sites on Platinum Nanoparticles for CO Oxidation: A Combined in Situ Spectroscopic and ab Initio Density Functional Theory Study. *Acs Catalysis* **9**, 7759-7768, doi:10.1021/acscatal.9b02552 (2019).
- 28 Suchorski, Y. *et al.* The role of metal/oxide interfaces for long-range metal particle activation during CO oxidation. *Nat. Mater.* **17**, 519+, doi:10.1038/s41563-018-0080-y (2018).
- 29 Hanukovich, S., Dang, A. & Christopher, P. Influence of Metal Oxide Support Acid Sites on Cu-Catalyzed Nonoxidative Dehydrogenation of Ethanol to Acetaldehyde. *Acs Catalysis* **9**, 3537-3550, doi:10.1021/acscatal.8b05075 (2019).
- 30 Ganzler, A. M. *et al.* Tuning the Pt/CeO₂ Interface by in Situ Variation of the Pt Particle Size. *Acs Catalysis* **8**, 4800-4811, doi:10.1021/acscatal.8b00330 (2018).
- 31 Murata, K. *et al.* Identification of active sites in CO oxidation over a Pd/Al₂O₃ catalyst. *Physical Chemistry Chemical Physics* **21**, 18128-18137, doi:10.1039/c9cp03943k (2019).
- 32 Cargnello, M. *et al.* Control of Metal Nanocrystal Size Reveals Metal-Support Interface Role for Ceria Catalysts. *Science* **341**, 771-773, doi:10.1126/science.1240148 (2013).

- 33 Hansen, T. W., Delariva, A. T., Challa, S. R. & Datye, A. K. Sintering of Catalytic Nanoparticles: Particle Migration or Ostwald Ripening? *Acc. Chem. Res.* **46**, 1720-1730, doi:10.1021/ar3002427 (2013).
- 34 Cargnello, M. *et al.* Exceptional Activity for Methane Combustion over Modular Pd@CeO₂ Subunits on Functionalized Al₂O₃. *Science* **337**, 713-717, doi:10.1126/science.1222887 (2012).
- 35 Zhang, F. *et al.* In Situ Elucidation of the Active State of Co-CeO_x Catalysts in the Dry Reforming of Methane: The Important Role of the Reducible Oxide Support and Interactions with Cobalt. *Acs Catalysis* **8**, 3550-3560, doi:10.1021/acscatal.7b03640 (2018).
- 36 Seo, J., Lee, S., Koo, B. & Jung, W. Controlling the size of Pt nanoparticles with a cationic surfactant, C_nTABr. *Cryst. Eng. Comm.* **20**, 2010-2015 (2018).
- 37 Lee, S., Seo, J. & Jung, W. Sintering-resistant Pt@CeO₂ nanoparticles for high-temperature oxidation catalysis. *Nanoscale* **8**, 10219-10228, doi:10.1039/c6nr00170j (2016).
- 38 Joo, S. H. *et al.* Thermally stable Pt/mesoporous silica core-shell nanocatalysts for high-temperature reactions. *Nat. Mater.* **8**, 126-131, doi:10.1038/nmat2329 (2009).
- 39 Kim, S., Lee, S. & Jung, W. Sintering Resistance of Pt@SiO₂ Core-Shell Catalyst. *ChemCatChem* **11**, 4653-4659, doi:10.1002/cctc.201900934 (2019).
- 40 Wang, Z. L. Transmission electron microscopy of shape-controlled nanocrystals and their assemblies. *J. Phys. Chem. B* **104**, 1153-1175, doi:10.1021/jp993593c (2000).
- 41 Zhang, S. *et al.* Dynamic structural evolution of supported palladium–ceria core–shell catalysts revealed by in situ electron microscopy. *Nature Communications* **6**, 7778, doi:10.1038/ncomms8778 (2015).
- 42 Jones, J. *et al.* Thermally stable single-atom platinum-on-ceria catalysts via atom trapping. *Science* **353**, 150, doi:10.1126/science.aaf8800 (2016).
- 43 Pereira-Hernández, X. I. *et al.* Tuning Pt-CeO₂ interactions by high-temperature vapor-phase synthesis for improved reducibility of lattice oxygen. *Nature Communications* **10**, 1358, doi:10.1038/s41467-019-09308-5 (2019).
- 44 Kunwar, D. *et al.* Stabilizing High Metal Loadings of Thermally Stable Platinum Single Atoms on an Industrial Catalyst Support. *ACS Catalysis* **9**, 3978-3990, doi:10.1021/acscatal.8b04885 (2019).
- 45 Klug, A. & Crowther, R. A. Three-dimensional Image Reconstruction from the Viewpoint of information Theory. *Nature* **238**, 435-440, doi:10.1038/238435a0 (1972).
- 46 Riscoe, A. R. *et al.* Transition state and product diffusion control by polymer–nanocrystal hybrid catalysts. *Nature Catalysis* **2**, 852-863, doi:10.1038/s41929-019-0322-7 (2019).

- 47 Nguyen, T. S. *et al.* Correlation of the ratio of metallic to oxide species with activity of PdPt catalysts for methane oxidation. *Catalysis Science & Technology* **10**, 1408-1421, doi:10.1039/C9CY02371B (2020).
- 48 Tao, F. F. *et al.* Understanding complete oxidation of methane on spinel oxides at a molecular level. *Nature Communications* **6**, doi:10.1038/ncomms8798 (2015).
- 49 Arai, H., Yamada, T., Eguchi, K. & Seiyama, T. CATALYTIC COMBUSTION OF METHANE OVER VARIOUS PEROVSKITE-TYPE OXIDES. *Appl. Catal.* **26**, 265-276, doi:10.1016/s0166-9834(00)82556-7 (1986).
- 50 Yao, Y. F. Y. OXIDATION OF ALKANES OVER NOBLE-METAL CATALYSTS. *Ind. Eng. Chem. Prod. Res. Dev.* **19**, 293-298, doi:10.1021/i360075a003 (1980).
- 51 Wang, X. & Gorte, R. J. A study of steam reforming of hydrocarbon fuels on Pd/ceria. *Appl. Catal. A Gen.* **224**, 209-218, doi:10.1016/s0926-860x(01)00783-9 (2002).
- 52 Tang, W. *et al.* Methane complete and partial oxidation catalyzed by Pt-doped CeO₂. *J. Catal.* **273**, 125-137, doi:10.1016/j.jcat.2010.05.005 (2010).
- 53 Lustemberg, P. G. *et al.* Room-Temperature Activation of Methane and Dry Re-forming with CO₂ on Ni-CeO₂(111) Surfaces: Effect of Ce³⁺ Sites and Metal-Support Interactions on C-H Bond Cleavage. *ACS Catalysis* **6**, 8184-8191, doi:10.1021/acscatal.6b02360 (2016).
- 54 Chin, Y. H., Buda, C., Neurock, M. & Iglesia, E. Reactivity of Chemisorbed Oxygen Atoms and Their Catalytic Consequences during CH₄-O₂ Catalysis on Supported Pt Clusters. *J. Am. Chem. Soc.* **133**, 15958-15978, doi:10.1021/ja202411v (2011).
- 55 Vincent, L. & Soille, P. WATERSHEDS IN DIGITAL SPACES - AN EFFICIENT ALGORITHM BASED ON IMMERSION SIMULATIONS. *Ieee Transactions on Pattern Analysis and Machine Intelligence* **13**, 583-598, doi:10.1109/34.87344 (1991).
- 56 Penczek, P., Marko, M., Buttle, K. & Frank, J. DOUBLE-TILT ELECTRON TOMOGRAPHY. *Ultramicroscopy* **60**, 393-410, doi:10.1016/0304-3991(95)00078-x (1995).
- 57 Mastronarde, D. N. Dual-axis tomography: An approach with alignment methods that preserve resolution. *Journal of Structural Biology* **120**, 343-352, doi:10.1006/jsbi.1997.3919 (1997).
- 58 Frangakis, A. S. & Hegerl, R. Noise reduction in electron tomographic reconstructions using nonlinear anisotropic diffusion. *Journal of Structural Biology* **135**, 239-250, doi:10.1006/jsbi.2001.4406 (2001).
- 59 Weyland, M. Electron tomography of catalysts. *Topics in Catalysis* **21**, 175-183, doi:10.1023/a:1021385427655 (2002).

- 60 Perona, P. & Malik, J. SCALE-SPACE AND EDGE-DETECTION USING ANISOTROPIC DIFFUSION. *Ieee Transactions on Pattern Analysis and Machine Intelligence* **12**, 629-639, doi:10.1109/34.56205 (1990).
- 61 Midgley, P. A. & Weyland, M. 3D electron microscopy in the physical sciences: the development of Z-contrast and EFTEM tomography. *Ultramicroscopy* **96**, 413-431, doi:10.1016/s0304-3991(03)00105-0 (2003).
- 62 Holzer, L., Indutnyi, F., Gasser, P. H., Munch, B. & Wegmann, M. Three-dimensional analysis of porous BaTiO₃ ceramics using FIB nanotomography. *Journal of Microscopy-Oxford* **216**, 84-95, doi:10.1111/j.0022-2720.2004.01397.x (2004).
- 63 Fernandez, J. J. & Li, S. Anisotropic nonlinear filtering of cellular structures in cryoelectron tomography. *Computing in Science & Engineering* **7**, 54-61, doi:10.1109/mcse.2005.89 (2005).
- 64 Yates, T. J. V. *et al.* Three-dimensional real-space crystallography of MCM-48 mesoporous silica revealed by scanning transmission electron tomography. *Chemical Physics Letters* **418**, 540-543, doi:10.1016/j.cplett.2005.11.031 (2006).
- 65 Ward, E. P. W., Yates, T. J. V., Fernandez, J. J., Vaughan, D. E. W. & Midgley, P. A. Three-dimensional nanoparticle distribution and local curvature of heterogeneous catalysts revealed by electron tomography. *Journal of Physical Chemistry C* **111**, 11501-11505, doi:10.1021/jp072441b (2007).
- 66 Prieto, G., Zecevic, J., Friedrich, H., de Jong, K. P. & de Jongh, P. E. Towards stable catalysts by controlling collective properties of supported metal nanoparticles. *Nat. Mater.* **12**, 34-39, doi:10.1038/nmat3471 (2013).
- 67 Goris, B. *et al.* Measuring Lattice Strain in Three Dimensions through Electron Microscopy. *Nano Letters* **15**, 6996-7001, doi:10.1021/acs.nanolett.5b03008 (2015).
- 68 Haberfehlner, G. *et al.* Formation of bimetallic clusters in superfluid helium nanodroplets analysed by atomic resolution electron tomography. *Nature Communications* **6**, doi:10.1038/ncomms9779 (2015).
- 69 Saha, P. K., Borgefors, G. & di Baja, G. S. A survey on skeletonization algorithms and their applications. *Pattern Recognition Letters* **76**, 3-12, doi:10.1016/j.patrec.2015.04.006 (2016).
- 70 Brunauer, S., Emmett, P. H. & Teller, E. Adsorption of Gases in Multimolecular Layers. *J. Am. Chem. Soc.* **60**, 309-319, doi:10.1021/ja01269a023 (1938).
- 71 Gilbert, P. Iterative methods for the three-dimensional reconstruction of an object from projections. *Journal of Theoretical Biology* **36**, 105-117, doi:https://doi.org/10.1016/0022-5193(72)90180-4 (1972).
- 72 Pizer, S. M. *et al.* ADAPTIVE HISTOGRAM EQUALIZATION AND ITS VARIATIONS. *Computer Vision Graphics and Image Processing* **39**, 355-368, doi:10.1016/s0734-189x(87)80186-x (1987).

- 73 van Heel, M. & Schatz, M. Fourier shell correlation threshold criteria. *Journal of Structural Biology* **151**, 250-262, doi:<https://doi.org/10.1016/j.jsb.2005.05.009> (2005).
- 74 Nieuwenhuizen, R. P. J. *et al.* Measuring image resolution in optical nanoscopy. *Nature Methods* **10**, 557-562, doi:[10.1038/nmeth.2448](https://doi.org/10.1038/nmeth.2448) (2013).
- 75 Kresse, G. & Furthmuller, J. Efficiency of ab-initio total energy calculations for metals and semiconductors using a plane-wave basis set. *Computational Materials Science* **6**, 15-50, doi:[10.1016/0927-0256\(96\)00008-0](https://doi.org/10.1016/0927-0256(96)00008-0) (1996).
- 76 Perdew, J. P., Burke, K. & Ernzerhof, M. Generalized gradient approximation made simple. *Physical Review Letters* **77**, 3865-3868, doi:[10.1103/PhysRevLett.77.3865](https://doi.org/10.1103/PhysRevLett.77.3865) (1996).
- 77 Dudarev, S. L., Botton, G. A., Savrasov, S. Y., Humphreys, C. J. & Sutton, A. P. Electron-energy-loss spectra and the structural stability of nickel oxide: An LSDA+U study. *Physical Review B* **57**, 1505-1509, doi:[10.1103/PhysRevB.57.1505](https://doi.org/10.1103/PhysRevB.57.1505) (1998).
- 78 Kim, H. Y., Lee, H. M. & Henkelman, G. CO Oxidation Mechanism on CeO₂-Supported Au Nanoparticles. *J. Am. Chem. Soc.* **134**, 1560-1570, doi:[10.1021/ja207510v](https://doi.org/10.1021/ja207510v) (2012).
- 79 Blochl, P. E. PROJECTOR AUGMENTED-WAVE METHOD. *Physical Review B* **50**, 17953-17979, doi:[10.1103/PhysRevB.50.17953](https://doi.org/10.1103/PhysRevB.50.17953) (1994).
- 80 Henkelman, G., Uberuaga, B. P. & Jonsson, H. A climbing image nudged elastic band method for finding saddle points and minimum energy paths. *Journal of Chemical Physics* **113**, 9901-9904, doi:[10.1063/1.1329672](https://doi.org/10.1063/1.1329672) (2000).

Figures

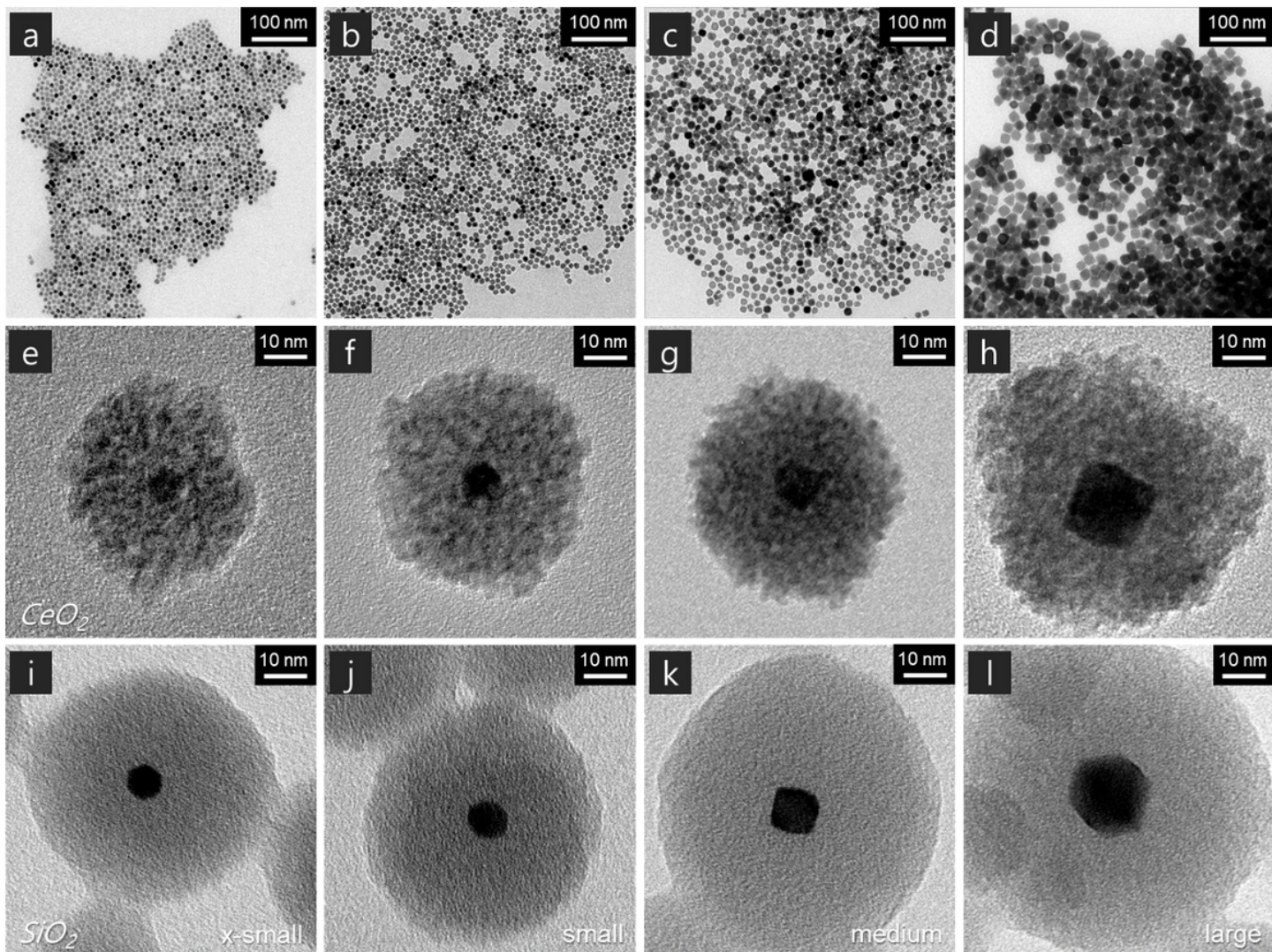


Figure 1

Morphology of as-prepared catalysts. TEM images of (a to d) Pt nanoparticles (NPs) with different particle sizes, (e to h) Pt@CeO₂, and (i to l) Pt@SiO₂ catalysts. Pt NP sizes are referred to as (a, e, i) x-small, (b, f, j) small, (c, g, k) medium, and (d, h, l) large.

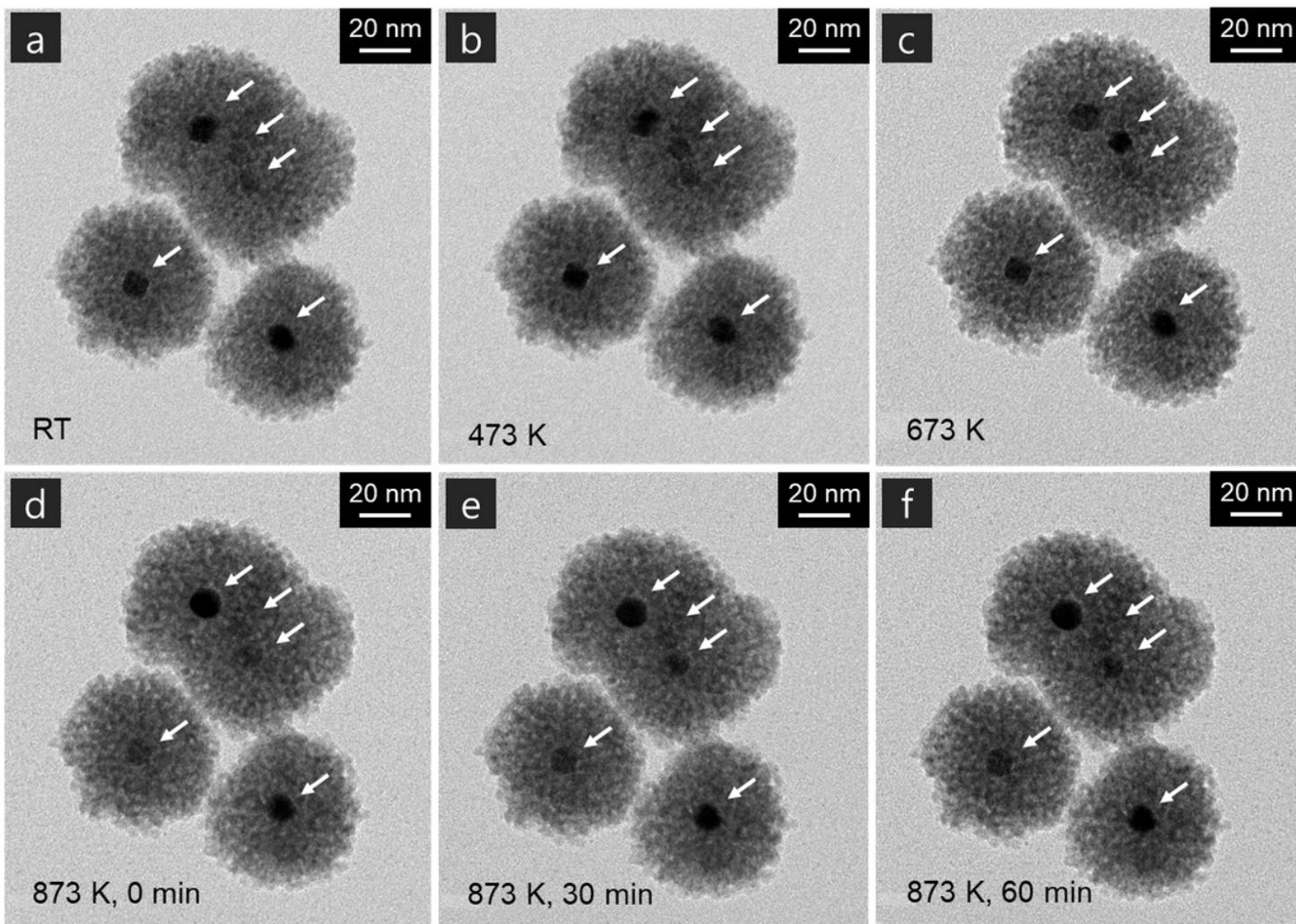


Figure 2

In-situ heating TEM analyses. In-situ TEM images of the Pt@CeO₂ catalyst under different temperature conditions: (a) room temperature (RT, 298 K), (b) 473 K, (c) 673 K, and (d) 873 K. TEM images of Pt@CeO₂ catalysts after constant-temperature annealing: (e) 30 minutes and (f) 60 minutes at 873 K.

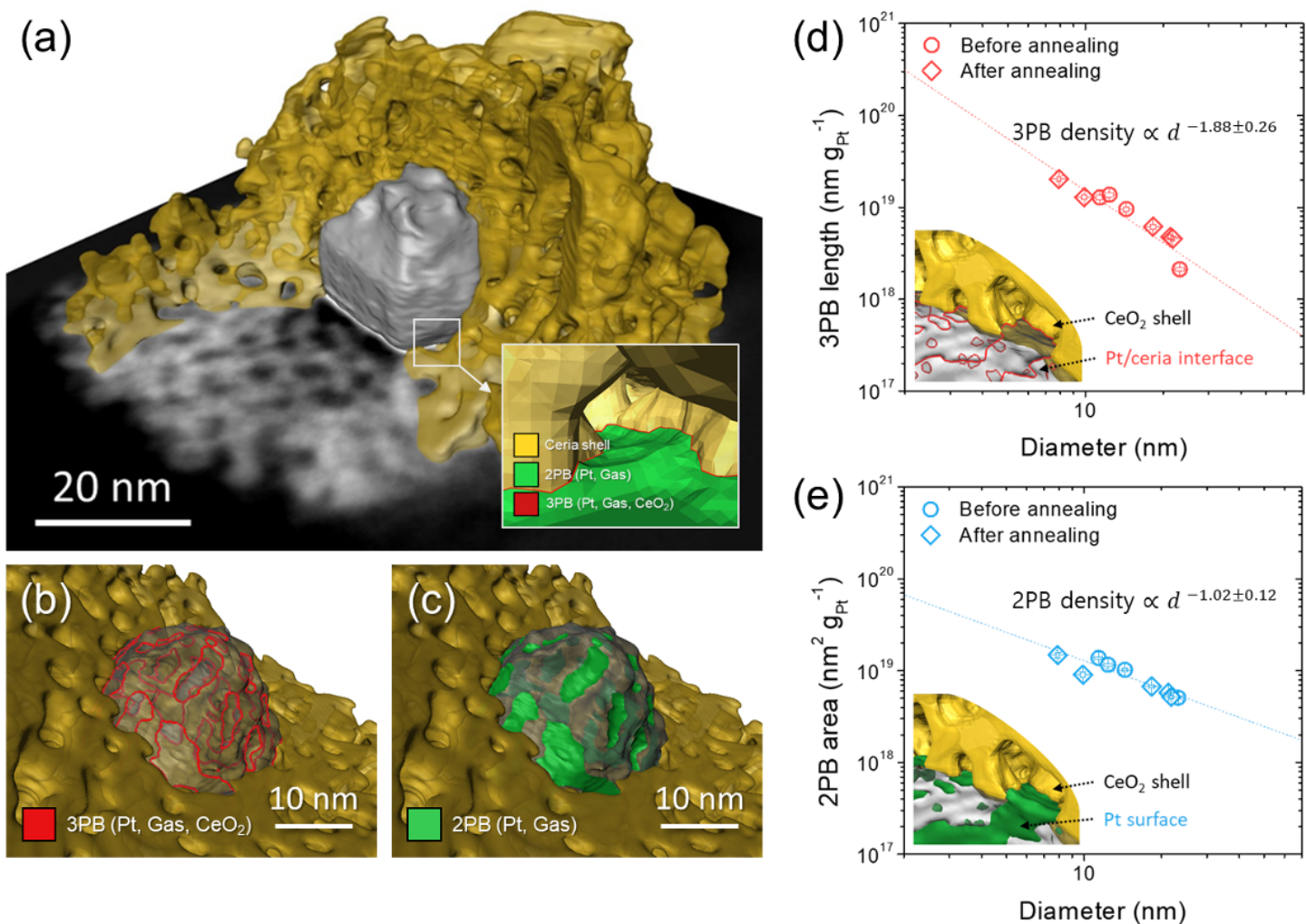


Figure 3

3D electron tomography. (a) Surface rendered Pt@CeO₂ configuration with a porous ceria shell (yellow) and a Pt NP (gray). The inset image presents a magnified view of the Pt@CeO₂ structure near the interface region between the ceria and Pt. The yellow surface is ceria and the green surface is Pt. The red line indicates the interface site. The cross-section image shows the (b) triple-phase boundary (red line) and (c) two-phase boundary (green surface). Variation of (d) the 3PB length and (e) 2PB area per gram of Pt plotted as a function of the Pt NP size. The 3PB length was estimated as the total length of a Pt voxel in contact with ceria. The 2PB area was measured as the total area of a Pt voxel in contact with a pore. Error bars indicate standard errors for estimated particle size, 2PB area, and 3PB length.

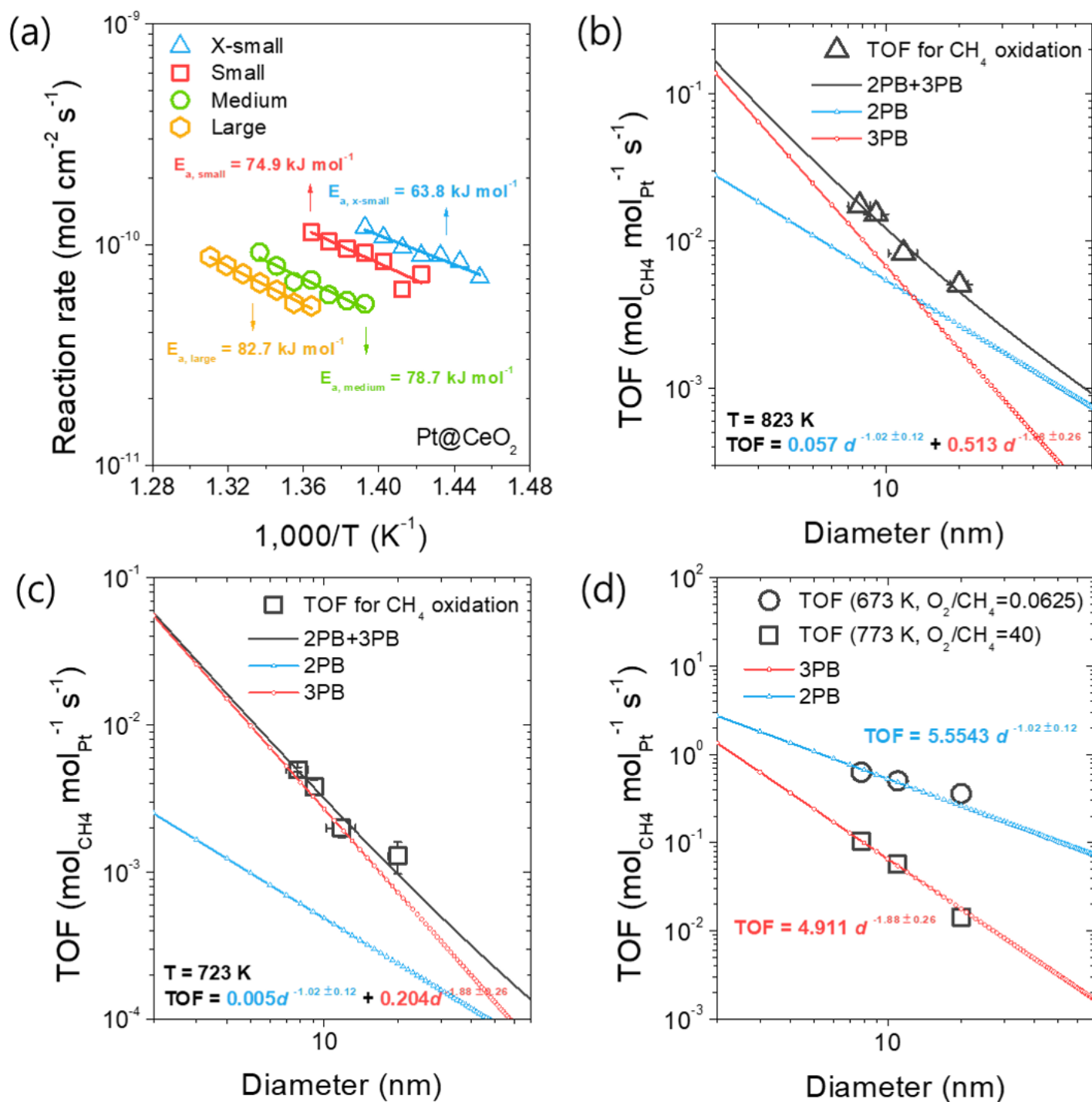


Figure 4

Size-dependent activities. (a) Arrhenius-type plot of CH₄ oxidation over CeO₂-encapsulated Pt catalysts. Reaction rates are normalized by the exposed metal surface area as identified from a CO chemisorption analysis. Turnover frequency (TOF) values of Pt@CeO₂ catalysts for CH₄ oxidation measured at (b) 823 K (black open triangle symbols) and (c) 723 K (black open square symbols). TOF values were fitted to the solid black line. The blue line with open triangle symbols and the red line with open circle symbols represent the size-dependent density levels of the 2PB and 3PB, respectively. The O₂/CH₄ ratio of the

input gas is 4. (d) TOF values of CH₄ oxidation catalyzed by Pt@CeO₂ at an O₂/CH₄ ratio of 0.0625 at 673 K (black open circle symbols) and an O₂/CH₄ ratio of 40 at 773 K (black open square symbols). Error bars indicate standard errors for particle sizes and TOFs.

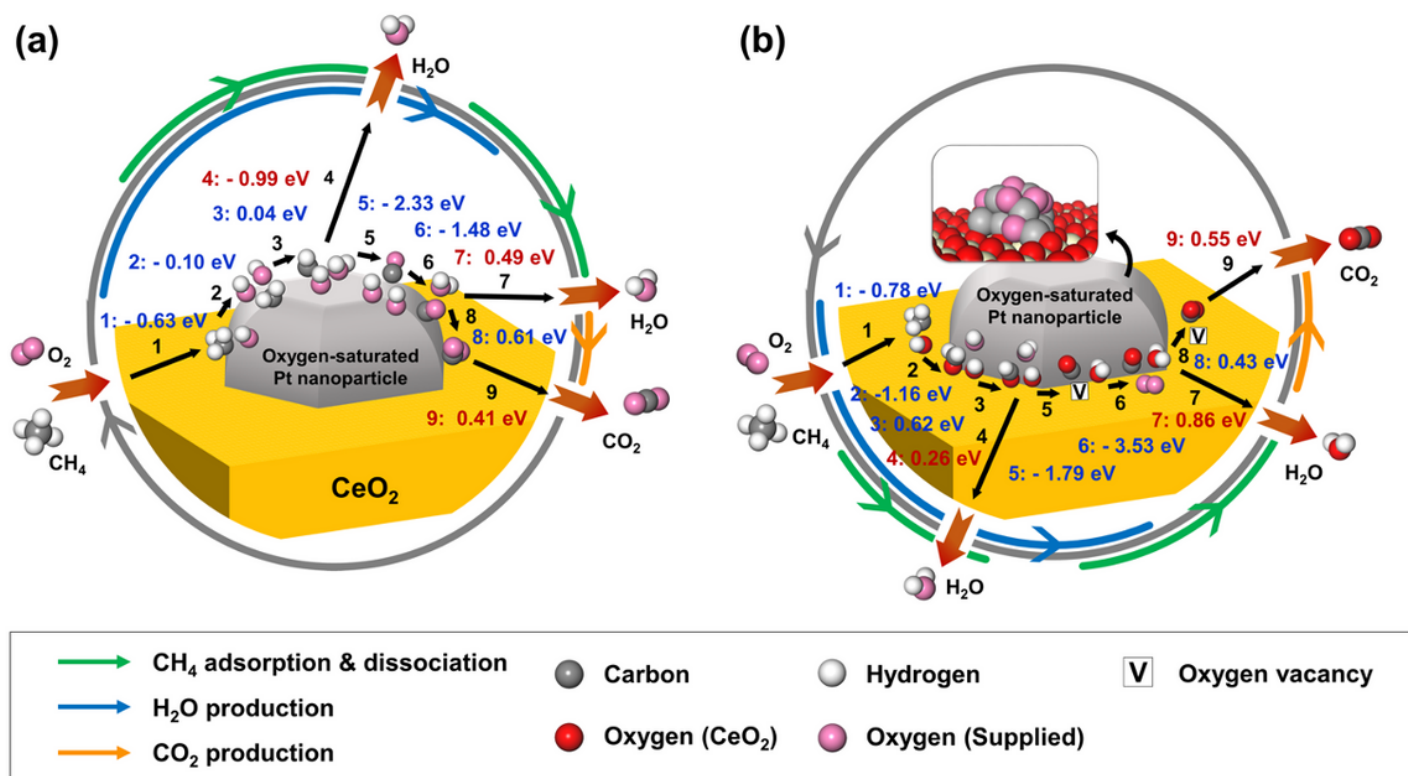


Figure 5

DFT-estimated CH₄ oxidation pathways. Schematic DFT-estimated CH₄ oxidation pathways catalyzed by (a) the 2PB and (b) the 3PB of Pt@CeO₂. Numbered black arrows denote the individual reaction steps of CH₄ oxidation. Corresponding reaction energy values are presented. Sequential 2PB reaction involves (a1) dissociative CH₄ adsorption, (a2) CH₃ dissociation, (a3) CH₂ dissociation and H₂O formation, (a4) 1st H₂O production (desorption), (a5) CH dissociation and CO formation, (a6) H₂O formation, (a7) 2nd H₂O production (desorption), (a8) CO₂ formation, and (a9) CO₂ production (desorption) pathways. In comparison, the 3PB reaction pathway consists of (b1) dissociative CH₄ adsorption, (b2) CH₃ dissociation, (b3) CH₂ dissociation and H₂O formation, (b4) 1st H₂O production (desorption), (b5) CH dissociation, CO and H₂O formation, (b6) vacancy healing, (b7) 2nd H₂O production (desorption), (b8) CO₂ formation, and (b9) CO₂ production (desorption). Refer to Fig. S19 and S20 for full reaction pathways and energetics.

Supplementary Files

This is a list of supplementary files associated with this preprint. Click to download.

- [21.01.28Supplementaryinformationsubmitted.pdf](#)

- 21.01.28VideoS1.PtXCeria.mp4